Annals of Mathematics and Computer Science ISSN: 2789-7206
Vol 37 (2026) 1-18 https://doi.org/10.56947/amcs.v37.976

PBH TRANSPORT AND GRAVITATIONAL-WAVE ANISOTROPY

BHAKTARAJ THIYAM[1,*]

Abstract. We develop a computational framework for primordial black-hole transport and its effect on supermassive black-hole binaries. A memory kernel couples dynamical friction, central-mass growth, residence time, gravitational-wave spectrum, and angular anisotropy. We formulate transport as a Volterra operator and establish positivity and stability under bounded coefficients. A time-discrete scheme is given with consistency estimate. An algorithm computes spectral and angular observables, including effective source number and a joint statistic. Direct memory evaluation is quadratic in time nodes, whereas a finite exponential-kernel representation is linear for fixed rank. The method recovers the no-PBH limit and provides a route for PTA tests.

Keywords. primordial black holes, dynamical friction, gravitational waves, numerical analysis, anisotropy
2020 Mathematics Subject Classification. Primary 65R20; Secondary 65L05

1. Introduction and computational motivation

Pulsar timing arrays (PTAs) have opened a new observational window on the nanohertz stochastic gravitational-wave background (SGWB). The NANOGrav, European Pulsar Timing Array, Parkes Pulsar Timing Array, and Chinese Pulsar Timing Array collaborations have reported evidence for a common-spectrum stochastic process and associated angular correlations [1, 2, 15, 17]. The standard astrophysical interpretation attributes a substantial part of the signal to a cosmological population of supermassive black-hole binaries (SMBHBs), while the Hellings–Downs correlation supplies the canonical angular response [8].

Primordial black holes (PBHs) provide an additional compact component that can participate in structure formation and, once embedded in dark-matter halos, can lose orbital energy through dynamical friction. The possible relevance of PBHs to early black-hole and galaxy formation has a long history [7, 4, 6]. Recent work has connected PBH transport and central-black-hole growth to the amplitude of the PTA SGWB [10]. Independently, the angular statistics of SMBHB backgrounds

Date: Received: Sep 28, 2026; Revised: Oct 25, 2026; Accepted: Nov 1, 2026.
* Corresponding author
© The Author(s) 2026. This article is licensed under a Creative Commons Attribution-NonCommercial-NoDerivatives 4.0 International License. To view a copy of the licence, visit https://creativecommons.org/licenses/by-nc-nd/4.0/.

have been shown to contain information about the number and relative strength of the contributing binaries [14].

The purpose of the present revision is to make the mathematical and computational content explicit. The central object is not merely a phenomenological sequence of astrophysical formulae. We formulate the memory-dependent central-growth relation as a causal Volterra operator, specify a numerical discretization, quantify its consistency and stability, and give an algorithm for mapping a population of halo realizations into spectral and angular observables. This emphasis is consistent with the mathematical-computational orientation of the *Annals of Mathematics and Computer Science*, particularly its interests in operator methods, numerical analysis, and computational methods for differential and integral equations. Recent AMCS papers illustrate this interface through operator-theoretic convergence analysis and numerical schemes for fractional or integro-differential equations [11, 16, 12].

The contribution is therefore methodological. The astrophysical ingredients are standard or explicitly phenomenological, whereas the proposed contribution is their organization into a causal integral operator together with a stable discretization and a computable source-weight map. No claim is made that the kernel itself is a new special function.

The model follows the causal chain

$$f_{\rm PBH} \longrightarrow \dot{M}_{\rm df} \longrightarrow M_\bullet \longrightarrow (M_1, M_2) \longrightarrow \mathcal{M} \longrightarrow \Omega_{\rm GW} \longrightarrow C_\ell. \tag{1.1}$$

Here $f_{\rm PBH}$ is the PBH mass fraction, $\dot{M}_{\rm df}$ is the transport rate, $M_\bullet$ is the central black-hole mass, $\mathcal{M}$ is the binary chirp mass, $\Omega_{\rm GW}$ is the spectral energy density, and C_ℓ denotes angular power.

The paper is organized as follows. Section 2 defines the transport source and the causal operator. Section 3 supplies the dynamical-friction closure. Section 4 derives the response-weighted SMBHB population. Section 5 constructs the SGWB spectrum. Section 6 defines the angular observables and the joint statistic. Section 7 gives the mathematical stability analysis. Section 8 describes the numerical discretization and algorithmic complexity. Section 9 presents limiting regimes and validation tests. Section 10 discusses parameter-space diagnostics and falsifiability. Sections 11 and 12 discuss interpretation and limitations, followed by conclusions.

2. PBH transport source

2.1. **Halo-associated PBH mass.** Consider a halo of mass $M(t)$ containing a PBH fraction $f_{\rm PBH}(t)$. The PBH mass associated with the halo is modeled by

$$M_{\rm PBH}(t) = f_{\rm PBH}(t)\frac{\Omega_{\rm CDM}(t)}{\Omega_m(t)}M(t). \tag{2.1}$$

The factor $\Omega_{\rm CDM}/\Omega_m$ allows the PBH fraction to be interpreted relative to the cold-dark-matter component.

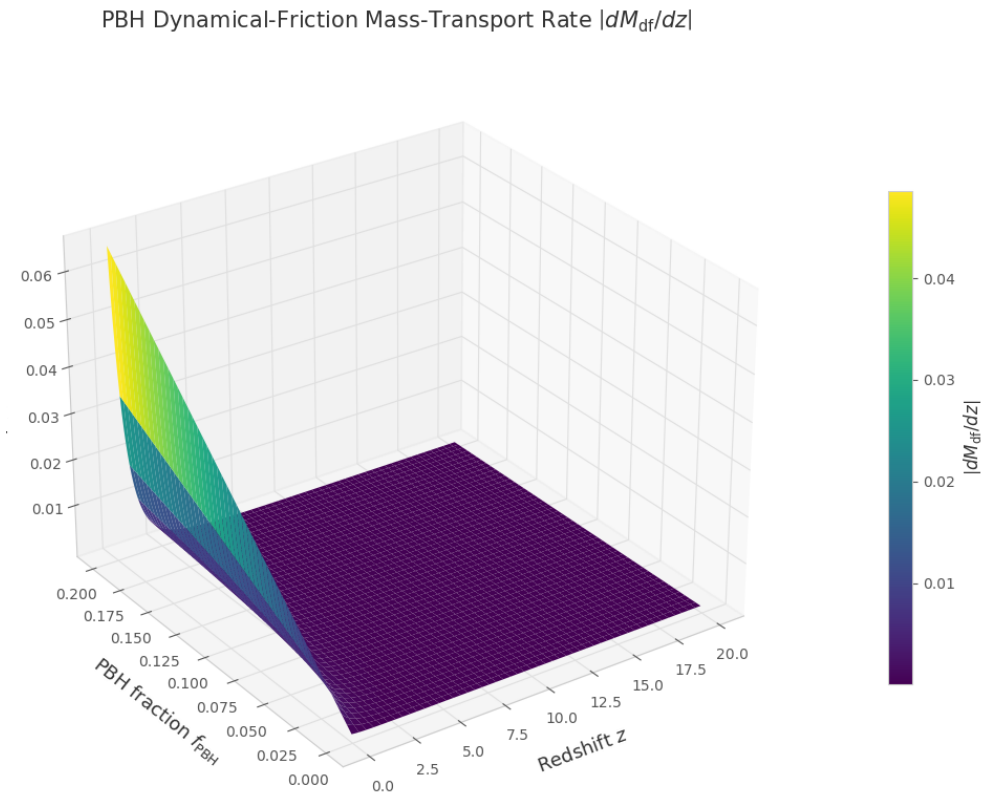


FIGURE 1. PBH Dynamical-Friction Mass-Transport Rate as a Function of Redshift and PBH Fraction

Only part of the PBH population reaches the central region. We write the transport efficiency as

$$\eta_{\rm df}(t) = F\left(J(t), \frac{m_\bullet(t)}{M(t)}, z(t)\right), \qquad 0 \le \eta_{\rm df}(t) \le 1, \tag{2.2}$$

where J is a dimensionless orbital-angular-momentum variable and $m_\bullet$ denotes the mass of an individual transported compact object.

The total transport time is

$$t_{\rm tr}(t) = t_{\rm df}(t) + t_{\rm merg}(t), \tag{2.3}$$

where $t_{\rm df}$ is the dynamical-friction time and $t_{\rm merg}$ is the merger delay.

Using

$$\frac{dt}{dz} = -\frac{1}{(1+z)H(z)}, \tag{2.4}$$

the PBH transport source may be written as

$$\frac{dM_{\rm df}}{dz} = -\frac{\eta_{\rm df}(z) f_{\rm PBH}(z)[\Omega_{\rm CDM}(z)/\Omega_m(z)]M(z)}{(1+z)H(z)t_{\rm tr}(z)}. \tag{2.5}$$

Equivalently, in cosmic time,

$$\dot{M}_{\rm df}(t) = \frac{\eta_{\rm df}(t) f_{\rm PBH}(t)[\Omega_{\rm CDM}(t)/\Omega_m(t)]M(t)}{t_{\rm tr}(t)}. \tag{2.6}$$

Equation (2.6) is a source relation rather than a complete population evolution law. Its role is to provide the forcing term for the central response operator introduced next.

3. Causal transport operator

3.1. **Kernel formulation.** A fixed delay does not describe a system in which the halo density, velocity dispersion, central mass, and orbital angular momentum evolve during transport. We therefore introduce a causal kernel

$$K(t,t') = K(t-t'; M(t'), M_\bullet(t'), \sigma(t'), J(t'), \rho(t'))\,, \tag{3.1}$$

with

$$K(t,t') = 0, \qquad t < t', \tag{3.2}$$

and

$$\int_{t'}^{\infty} K(t,t')\,dt = 1. \tag{3.3}$$

The normalization means that a transported mass element is redistributed in arrival time rather than created or destroyed by the kernel itself.

For a reference model, the memory kernel is

$$K_0(\Delta t) = \frac{1}{t_{\rm tr}} \exp\left(-\frac{\Delta t}{t_{\rm tr}}\right), \qquad \Delta t \geq 0. \tag{3.4}$$

The exponential kernel is used only as a benchmark. The generalized model permits the transport timescale and environmental arguments to vary along the trajectory.

3.2. **Central mass response.** Let $\dot{M}_{\rm gas}$ denote gas accretion and $\dot{M}_{\rm merg}$ the contribution from ordinary hierarchical mergers. The central growth rate is

$$\dot{M}_\bullet(t) = \dot{M}_{\rm gas}(t) + \dot{M}_{\rm merg}(t) + \int_{t_0}^{t} \dot{M}_{\rm df}(t') K(t,t')\,dt'. \tag{3.5}$$

The central mass is consequently

$$M_\bullet(t) = M_{\bullet,0} + \int_{t_0}^{t} \dot{M}_\bullet(s)\,ds. \tag{3.6}$$

Define the Volterra operator

$$(\mathcal{V}q)(t) = \int_{t_0}^{t} K(t,t') q(t')\,dt'. \tag{3.7}$$

Then the transport part of Eq. (3.5) is simply $\mathcal{V}\dot{M}_{\rm df}$. This representation is useful because the causal upper-triangular structure of the discrete operator permits sequential evaluation without solving a dense two-sided integral equation.

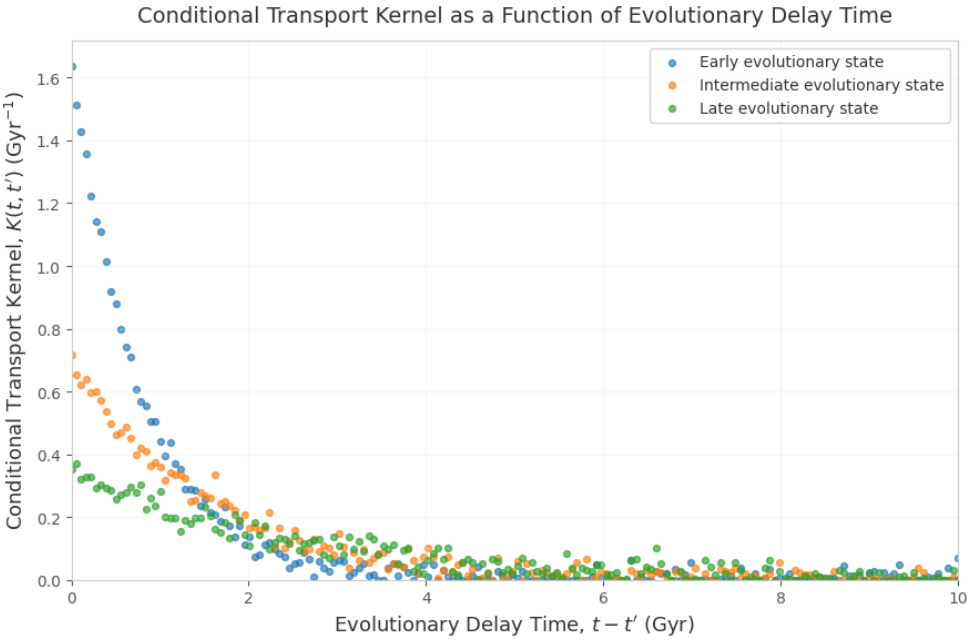


FIGURE 2. Conditional Transport Kernel as a Function of Evolutionary Delay Time

3.3. **Bounded-coefficient formulation.** For the numerical analysis, suppose that on a finite interval $I = [t_0, T]$,

$$0 \le K(t, t') \le K_{\max}, \qquad 0 \le q(t) \le q_{\max}, \qquad t_0 \le t' \le t \le T, \tag{3.8}$$

and that K is continuously differentiable in its first argument. Then

$$\|\mathcal{V}q\|_\infty \le K_{\max}(T - t_0)\|q\|_\infty. \tag{3.9}$$

For a normalized kernel, the sharper estimate

$$\|\mathcal{V}q\|_\infty \le \|q\|_\infty \tag{3.10}$$

holds whenever the integration interval contains the full normalized support of the kernel. Thus the transport operator does not amplify the sup-norm of a nonnegative source.

If two source functions q_1, q_2 are used with the same kernel, then

$$\|\mathcal{V}q_1 - \mathcal{V}q_2\|_\infty \le \|q_1 - q_2\|_\infty. \tag{3.11}$$

This stability property is the principal mathematical reason for retaining the causal integral form in the computation.

4. Dynamical-friction closure

4.1. **Chandrasekhar model.** For a compact object of mass $m_\bullet$ moving with speed v through a background of density ρ and velocity dispersion σ, the Chandrasekhar force is approximated by [5]

$$\mathbf{F}_{\rm df} = -4\pi G^2 m_\bullet^2 \rho \ln\Lambda \frac{F(X)}{v^3}\mathbf{v}, \tag{4.1}$$

where

$$X = \frac{v}{\sqrt{2}\sigma}, \qquad F(X) = \mathrm{erf}(X) - \frac{2X}{\sqrt{\pi}} e^{-X^2}. \tag{4.2}$$

A characteristic decay time is

$$t_{\rm df} \simeq \frac{v^3}{4\pi G^2 m_\bullet \rho \ln\Lambda F(X)}. \tag{4.3}$$

The scaling

$$t_{\rm df} \propto \frac{M}{m_\bullet \ln\Lambda} \tag{4.4}$$

makes the transport mass dependent.

The halo-scale approximation used in the original model can be retained as an optional closure,

$$t_{\rm df} \simeq H^{-1}(z) \left(\frac{\Delta_c(z)}{200}\right)^{-1} \left(\frac{J/J_c}{0.1}\right)^{0.01} \left(\frac{m_\bullet \ln\Lambda}{0.01M}\right)^{-1}. \tag{4.5}$$

The precise prefactor is model dependent; the numerical framework below only requires a positive computable $t_{\rm df}$.

4.2. **Transport efficiency and parameter dependence.** The parameter vector is

$$\Theta = \{f_{\rm PBH}, \eta_{\rm df}, z_{\rm df}, \ln\Lambda, t_{\rm merg}, \Theta_{\rm env}\}, \tag{4.6}$$

where $\Theta_{\rm env}$ controls environmental binary evolution.

The model separates three effects: the amount of PBH mass available, the fraction transported, and the time distribution of arrival. This separation is essential computationally because each factor enters a different stage of the pipeline.

5. Response-weighted SMBH population

5.1. **Population mapping.** Let i label SMBHBs. The transport model maps the halo population to a binary population through

$$P(M_1, M_2, z) = P[M_\bullet(M, z; f_{\rm PBH})]\, P(M_1, M_2 \mid M_\bullet, z). \tag{5.1}$$

The second factor contains the adopted pairing and mass-ratio prescription. Hierarchical halo-merger histories can be generated using standard merger prescriptions [9].

The chirp mass is

$$\mathcal{M} = \frac{(M_1 M_2)^{3/5}}{(M_1 + M_2)^{1/5}}. \tag{5.2}$$

The observed frequency f corresponds to rest-frame frequency

$$f_r = (1+z) f. \tag{5.3}$$



FIGURE 3. Binary Residence Time as a Function of Rest-Frame Gravitational-Wave Frequency

5.2. **Residence time.** The residence time is defined by

$$t_{\rm res}(f_r) = \left| \frac{d \ln f_r}{dt} \right|^{-1}. \tag{5.4}$$

For a circular GW-driven inspiral, the Peters timescale is [13]

$$t_{\rm GW}(f_r) = \frac{5c^5}{96 G^{5/3} \pi^{8/3} \mathcal{M}^{5/3} f_r^{8/3}}. \tag{5.5}$$

Environmental hardening may be represented by a timescale $t_{\rm env}$, giving

$$\frac{1}{t_{\rm res}} = \frac{1}{t_{\rm GW}} + \frac{1}{t_{\rm env}}. \tag{5.6}$$

The response-weighted differential population is

$$\frac{d^3 N_{\rm eff}}{dz\, dM_1\, dM_2} = \frac{d^3 R_{\rm BH}}{dz\, dM_1\, dM_2} t_{\rm res}(f_r). \tag{5.7}$$

This weighting is important because a source contributes to a frequency bin for a time determined by its orbital evolution.

6. GRAVITATIONAL-WAVE SPECTRUM

6.1. **Energy-density spectrum.** The SGWB energy density is

$$\Omega_{\rm GW}(f) = \frac{1}{\rho_c c^2} \frac{d\rho_{\rm GW}}{d \ln f}. \tag{6.1}$$

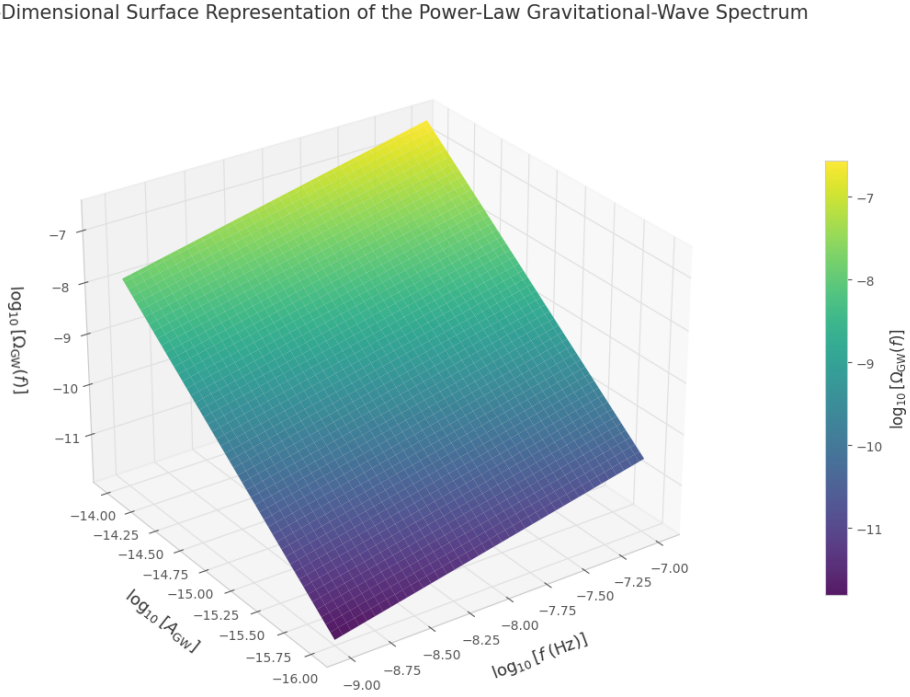


FIGURE 4. Three-Dimensional Surface Representation of the Power-Law Gravitational-Wave Spectrum

For a population of circular binaries,

$$h_c^2(f) \propto f^{-4/3} \int dz\, dM_1\, dM_2\, \frac{d^3 R_{\rm BH}}{dz\, dM_1\, dM_2} \mathcal{M}^{5/3} (1+z)^{-1/3}, \tag{6.2}$$

and

$$\Omega_{\rm GW}(f) = \frac{2\pi^2}{3H_0^2} f^2 h_c^2(f). \tag{6.3}$$

The familiar power-law limit is

$$h_c(f) = A_{\rm GW} \left(\frac{f}{f_{\rm yr}} \right)^{-2/3}. \tag{6.4}$$

6.2. **Transport response of the amplitude.** Let A_0 be the amplitude for the reference model with $f_{\rm PBH} = 0$, and $A_{\rm PBH}$ the amplitude of the transport model. Define

$$G_A(f_{\rm PBH}) = \frac{A_{\rm PBH}}{A_0}. \tag{6.5}$$

The leading mass dependence follows from the chirp-mass moment,

$$\left\langle \mathcal{M}^{5/3} \right\rangle_{\rm tr} = \frac{\int dz\, dM_1\, dM_2\, R_{\rm tr} \mathcal{M}^{5/3}}{\int dz\, dM_1\, dM_2\, R_{\rm tr}}. \tag{6.6}$$

A useful diagnostic approximation is

$$G_A \simeq \left[\frac{\langle \mathcal{M}^{5/3}\rangle_{\rm tr}}{\langle \mathcal{M}^{5/3}\rangle_0}\right]^{1/2} \left[\frac{R_{\rm tr}}{R_0}\right]^{1/2}, \tag{6.7}$$

where the expression is explicitly an approximation, not an identity.

7. Angular anisotropy and the joint observable

7.1. **Discrete source weights.** For a discrete realization, let $\Omega_i(f)$ denote the contribution of source i. Define

$$r_i(f) = \frac{\Omega_i(f)}{\Omega_{\rm tot}(f)}, \qquad \Omega_{\rm tot}(f) = \sum_{i=1}^{N} \Omega_i(f), \tag{7.1}$$

so that

$$\sum_{i=1}^{N} r_i(f) = 1. \tag{7.2}$$

The source weight used by the numerical implementation is

$$W_i(f) = \mathcal{M}_i^{5/3}(1+z_i)^{-1/3} t_{{\rm res},i}(f) R_i. \tag{7.3}$$

The normalized transport weight is

$$r_i^{\rm tr}(f) = \frac{W_i(f)}{\sum_{j=1}^{N} W_j(f)}. \tag{7.4}$$

7.2. **Multipoles.** For source directions $\hat{\mathbf{n}}_i$, define

$$c_{\ell m}(f) = \sum_{i=1}^{N} W_i(f) Y_{\ell m}(\hat{\mathbf{n}}_i). \tag{7.5}$$

The angular power spectrum is

$$C_\ell(f) = \frac{1}{2\ell+1} \sum_{m=-\ell}^{\ell} |c_{\ell m}(f)|^2. \tag{7.6}$$

For the monopole,

$$C_0(f) = \frac{\Omega_{\rm tot}^2(f)}{4\pi}. \tag{7.7}$$

The normalized angular statistic is therefore

$$A_\ell(f) = \frac{C_\ell(f)}{C_0(f)}. \tag{7.8}$$

Using the addition theorem for spherical harmonics gives the equivalent pair-sum representation

$$A_\ell(f) = \sum_{i,j=1}^{N} r_i(f) r_j(f) P_\ell(\hat{\mathbf{n}}_i \cdot \hat{\mathbf{n}}_j). \tag{7.9}$$

Since $|P_\ell(x)| \le 1$ for $x \in [-1,1]$,

$$0 \le A_\ell(f) \le 1. \tag{7.10}$$

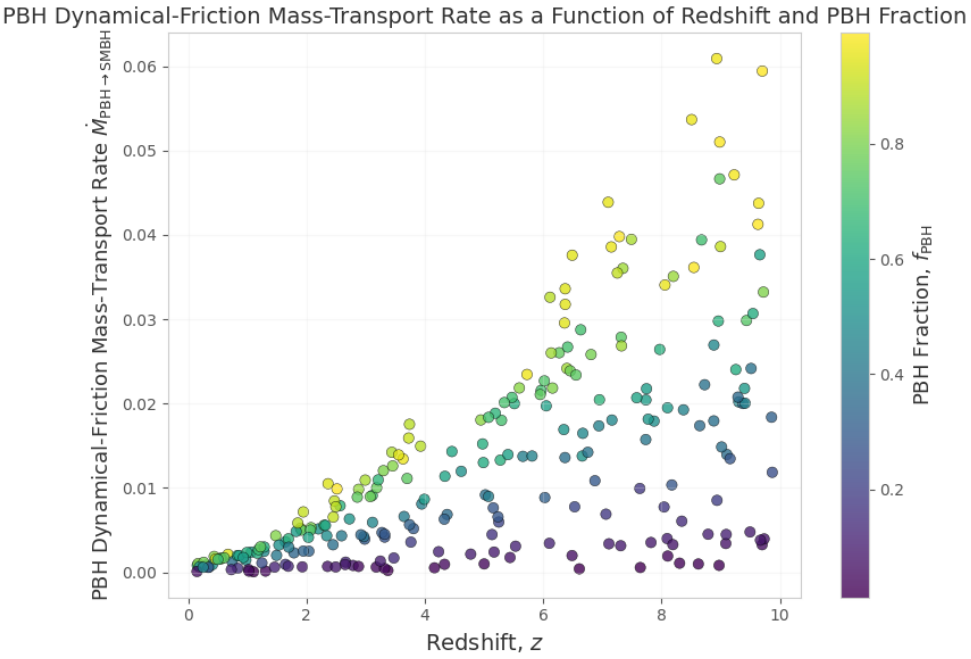


FIGURE 5. Redshift Dependence of PBH-Induced SMBH Mass Transport

The upper bound follows directly from the normalized source weights and provides a simple numerical sanity check.

7.3. **Effective source number.** A convenient concentration measure is

$$N_{\mathrm{eff}}(f) = \left[\sum_{i=1}^{N} r_i^2(f)\right]^{-1}. \tag{7.11}$$

A background dominated by a few loud binaries has smaller N_{eff} and generally larger realization-to-realization anisotropy. This is consistent with the statistical behavior found in recent SMBHB anisotropy studies [14].

7.4. **Joint spectral–anisotropy statistic.** We define

$$J_\ell(f) = \left[\frac{C_\ell^{\mathrm{tr}}(f)/C_0^{\mathrm{tr}}(f)}{C_\ell^{(0)}(f)/C_0^{(0)}(f)}\right]\left[\frac{\Omega_{\mathrm{GW}}^{\mathrm{tr}}(f)}{\Omega_{\mathrm{GW}}^{(0)}(f)}\right]^{-2}. \tag{7.12}$$

The exponent -2 is a normalization choice motivated by the quadratic dependence of angular power on source amplitudes. It is part of the definition of J_ℓ and is not asserted to follow as an independent identity.

In the no-PBH limit,

$$f_{\mathrm{PBH}} \to 0 \quad\Longrightarrow\quad M_\bullet \to M_\bullet^{(0)}, \quad \Omega_{\mathrm{GW}} \to \Omega_{\mathrm{GW}}^{(0)}, \quad A_\ell \to A_\ell^{(0)}, \quad J_\ell \to 1. \tag{7.13}$$

This gives a direct computational null test.

8. Mathematical stability of the transport discretization

8.1. **Time grid and quadrature.** Let

$$t_n = t_0 + nh, \qquad n = 0, \dots, N, \qquad h = \frac{T - t_0}{N}. \tag{8.1}$$

For the causal integral in Eq. (3.5), define

$$I_n = \int_{t_0}^{t_n} K(t_n, s) q(s)\, ds, \qquad q(s) = \dot{M}_{\rm df}(s). \tag{8.2}$$

The composite trapezoidal approximation is

$$I_n^{(h)} = h \left[\frac{1}{2} K_{n0} q_0 + \sum_{j=1}^{n-1} K_{nj} q_j + \frac{1}{2} K_{nn} q_n \right], \tag{8.3}$$

where $K_{nj} = K(t_n, t_j)$.

If $g_n(s) = K(t_n, s)q(s)$ has a bounded second derivative on $[t_0, t_n]$, then the standard quadrature estimate yields

$$|I_n - I_n^{(h)}| \le \frac{(t_n - t_0)h^2}{12} \max_{s \in [t_0, t_n]} \left| \frac{\partial^2 g_n}{\partial s^2}(s) \right|. \tag{8.4}$$

Hence the integral evaluation is second-order consistent under the stated smoothness condition.

8.2. **Sequential mass update.** Let

$$b(t) = \dot{M}_{\rm gas}(t) + \dot{M}_{\rm merg}(t). \tag{8.5}$$

A second-order predictor–corrector update for the central mass is

$$\widetilde{M}_{\bullet,n+1} = M_{\bullet,n} + h \left[b_n + I_n^{(h)} \right], \tag{8.6}$$

$$M_{\bullet,n+1} = M_{\bullet,n} + \frac{h}{2} \left[b_n + I_n^{(h)} + b_{n+1} + \widetilde{I}_{n+1}^{(h)} \right]. \tag{8.7}$$

Here $\widetilde{I}_{n+1}^{(h)}$ is evaluated using the predicted state. The causal structure means that only values with $j \le n + 1$ enter the update.

Assume that b, q, and the kernel are Lipschitz continuous and that the predictor remains in a bounded physical region. If the one-step consistency error is bounded by Ch^2, the discrete perturbation satisfies

$$|e_{n+1}| \le (1 + Lh)|e_n| + Ch^2, \tag{8.8}$$

where L is a bound on the local Lipschitz constant of the coupled right-hand side. Iteration gives

$$\max_{0 \le n \le N} |e_n| \le \frac{C}{L} \left(e^{L(T - t_0)} - 1 \right) h + e^{L(T - t_0)} |e_0|. \tag{8.9}$$

Thus the global mass error is $O(h)$ for this explicit predictor–corrector construction. If the corrector is iterated to convergence and the quadrature regularity assumptions hold, the observed order can approach second order.

The distinction between the local quadrature order and the global coupled update order is important for reproducibility: the integral approximation is second

order, but the complete algorithm should be reported as first-order globally unless the corrected state is iterated sufficiently to establish the higher-order regime.

8.3. **Positivity and numerical admissibility.** The physical variables satisfy

$$M_\bullet \geq 0, \qquad \dot{M}_{\rm df} \geq 0, \qquad 0 \leq \eta_{\rm df} \leq 1, \qquad K \geq 0. \tag{8.10}$$

A time step is rejected if the numerical update produces a negative mass, a negative transport rate, or a kernel whose discrete normalization differs from unity beyond the prescribed tolerance. The discrete kernel normalization is monitored by

$$\left| h \left[\frac{1}{2} K_{n0} + \sum_{j=1}^{n-1} K_{nj} + \frac{1}{2} K_{nn} \right] - 1 \right| \leq \varepsilon_K. \tag{8.11}$$

This provides a direct implementation-level validation criterion.

9. Numerical algorithm and complexity

9.1. **Population-evolution pipeline.** For each halo realization the computation proceeds in the following order:

$$f_{\rm PBH} \to M_{\rm PBH} \to t_{\rm df} \to \dot{M}_{\rm df} \to \mathcal{V}\dot{M}_{\rm df} \to M_\bullet \to (M_1, M_2) \to \mathcal{M} \to t_{\rm res} \to W_i \to \{\Omega_{\rm GW}, C_\ell, N_{\rm eff}, J_\ell\}. \tag{9.1}$$

For a grid of N_t time points and direct evaluation of the causal memory integral, the number of kernel-source products is

$$\sum_{n=1}^{N_t} n = \frac{N_t(N_t+1)}{2} = O(N_t^2). \tag{9.2}$$

The memory requirement is $O(N_t)$ if only the current accumulated integral is stored, or $O(N_t^2)$ if the full kernel matrix is retained.

9.2. **Finite exponential representation.** For long memory histories, the kernel can be approximated by a positive finite sum

$$K(t,t') \simeq \sum_{k=1}^{K} a_k \exp[-\lambda_k (t-t')]\, \mathbf{1}_{t \geq t'}, \qquad a_k \geq 0, \quad \lambda_k > 0. \tag{9.3}$$

Define auxiliary states

$$u_k(t) = \int_{t_0}^{t} a_k e^{-\lambda_k (t-s)} q(s)\, ds. \tag{9.4}$$

Differentiation gives

$$\dot{u}_k(t) = a_k q(t) - \lambda_k u_k(t), \qquad u_k(t_0) = 0, \tag{9.5}$$

and therefore

$$(\mathcal{V}q)(t) \simeq \sum_{k=1}^{K} u_k(t). \tag{9.6}$$

The memory computation is now replaced by K scalar recurrences per time step, giving

$$\text{cost} = O(KN_t), \qquad \text{memory} = O(KN_t) \tag{9.7}$$

for stored trajectories, or $O(K)$ when only the current auxiliary states are required. This is the main computational reduction of the operator formulation.

9.3. **Discrete source realization.** For N_s binaries, the weights are evaluated at frequencies f_q, $q = 1, \ldots, N_f$. The direct spectral accumulation has cost

$$O(N_s N_f), \tag{9.8}$$

while evaluating all pair sums in Eq. (7.9) costs

$$O(N_s^2 N_f) \tag{9.9}$$

for each set of multipoles. The spherical-harmonic route in Eq. (7.5) reduces this to approximately

$$O(N_s N_f \ell_{\max}^2) \tag{9.10}$$

when all m modes through $\ell_{\max}$ are retained.

The complete numerical workflow is therefore modular: the transport solver controls the mass history, the population sampler maps that history to binaries, and the angular module converts source weights into multipoles. Each module can be independently validated.

9.4. **Pseudocode.** The computational procedure can be summarized as follows.

(1) Choose Θ, a redshift interval, a time grid, and a frequency grid.
(2) Generate or read halo histories $M(z)$, $\rho(z)$, $\sigma(z)$ and angular-momentum variables $J(z)$.
(3) Compute $M_{\rm PBH}$, $\eta_{\rm df}$, $t_{\rm df}$ and $t_{\rm tr}$.
(4) Evaluate $\dot{M}_{\rm df}$ from Eq. (2.6).
(5) Evaluate the causal convolution using Eq. (8.3), or the exponential-state representation in Eq. (9.5).
(6) Update $M_\bullet$ and reject a step if physical positivity or kernel-normalization tests fail.
(7) Sample (M_1, M_2, z) from the evolved population prescription.
(8) Compute $\mathcal{M}$, $t_{\rm res}$, and the source weights $W_i(f)$.
(9) Normalize the weights, compute $\Omega_{\rm GW}$, C_ℓ/C_0, and $N_{\rm eff}$.
(10) Repeat for the reference case $f_{\rm PBH} = 0$ and evaluate J_ℓ.
(11) Perform grid refinement and Monte Carlo replication before comparing with observational constraints.

10. Validation and limiting regimes

10.1. **No-PBH limit.** As

$$f_{\rm PBH} \to 0, \tag{10.1}$$

we have

$$\dot{M}_{\rm df} \to 0, \qquad M_\bullet \to M_\bullet^{(0)}, \qquad \Omega_{\rm GW} \to \Omega_{\rm GW}^{(0)}. \tag{10.2}$$

The numerical implementation must reproduce this limit to within the chosen solver tolerance.

10.2. **Weak dynamical friction.** When

$$t_{\rm df} \gg t_{\rm merg}, \tag{10.3}$$

the transport time satisfies $t_{\rm tr} \simeq t_{\rm df}$ and

$$\dot{M}_{\rm df} \simeq \frac{\eta_{\rm df} f_{\rm PBH}(\Omega_{\rm CDM}/\Omega_m) M}{t_{\rm df}}. \tag{10.4}$$

The PBH contribution is therefore suppressed.

10.3. **Rapid dynamical friction.** When

$$t_{\rm df} \ll t_{\rm merg}, \tag{10.5}$$

one has $t_{\rm tr} \simeq t_{\rm merg}$ and

$$\dot{M}_{\rm df} \simeq \frac{\eta_{\rm df} f_{\rm PBH}(\Omega_{\rm CDM}/\Omega_m) M}{t_{\rm merg}}. \tag{10.6}$$

This regime provides a useful upper-response benchmark for fixed $\eta_{\rm df}$.

10.4. **Merger-dominated transport.** If the merger delay is much longer than the friction time, the same limiting relation as Eq. (10.6) follows. Conversely, if merger delays are short, friction controls the arrival rate. These checks must be recovered numerically when the dimensionless ratios

$$\chi_{\rm df} = \frac{t_{\rm df}}{t_{\rm merg}}, \qquad \chi_{\rm env} = \frac{t_{\rm GW}}{t_{\rm env}} \tag{10.7}$$

are driven to asymptotic values.

10.5. **Grid-convergence test.** Let Q_h denote any computed observable, such as A_ℓ, $N_{\rm eff}$, or J_ℓ. A practical refinement test is

$$E_h = \frac{|Q_h - Q_{h/2}|}{\max(1, |Q_{h/2}|)}. \tag{10.8}$$

For a first-order globally convergent implementation,

$$\frac{E_h}{E_{h/2}} \approx 2, \tag{10.9}$$

whereas a second-order regime gives an approximate factor of four. This test should be reported together with the physical parameter values and the random seed used for discrete source realizations.

11. Parameter-space predictions

The primary observables are

$$\{A_{\rm GW}, A_1, A_2, A_3, N_{\rm eff}, J_1, J_2\} = \mathcal{F}(\Theta). \tag{11.1}$$

A parameter scan should therefore not be restricted to the SGWB amplitude. It should simultaneously monitor the angular response and the effective source concentration.

The first constraint is a spectral condition,

$$A_{\rm obs}^{\rm min} \leq A_{\rm GW}(\Theta) \leq A_{\rm obs}^{\rm max}, \tag{11.2}$$

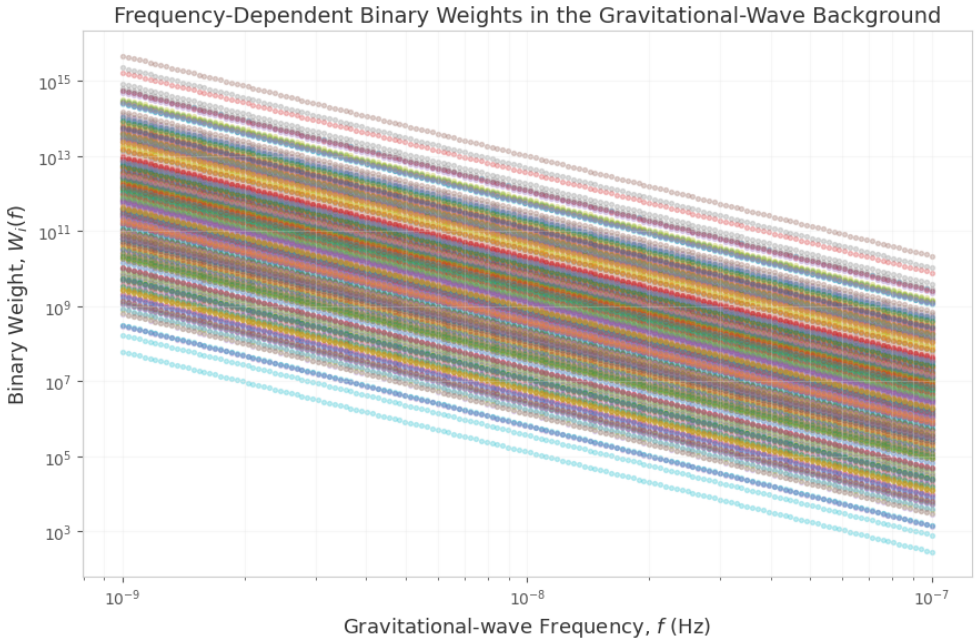


FIGURE 6. Frequency-Dependent Binary Weights in the Gravitational-Wave Background

while angular measurements impose

$$A_\ell(\Theta) \leq A_\ell^{\max}, \qquad \ell \geq 1. \tag{11.3}$$

These hard bounds are only screening conditions. A statistically complete analysis must replace them by the full PTA likelihood, including timing noise, pulsar distribution, Hellings–Downs correlations, frequency covariance, and the anisotropy likelihood.

12. Expected spectral–anisotropy response

12.1. **Mass-growth channel.** The transport model gives the qualitative sequence

$$f_{\rm PBH} \uparrow \Longrightarrow M_\bullet \uparrow \Longrightarrow \mathcal{M} \uparrow . \tag{12.1}$$

Because the leading circular-inspiral contribution scales as $\mathcal{M}^{5/3}$, an increased chirp-mass moment can enhance the SGWB amplitude.

12.2. **Source-concentration channel.** If the mass growth is concentrated in the loudest systems, then their relative weights can increase:

$$\mathcal{M}_{\max} \uparrow \Longrightarrow r_{\max} \uparrow \Longrightarrow N_{\rm eff} \downarrow . \tag{12.2}$$

A lower effective source number generally increases the importance of discrete-source fluctuations and can enhance the observed anisotropy. The sign and magnitude of the correlation must, however, be obtained from the actual population realization rather than imposed analytically.

12.3. **Small-PBH response.** For sufficiently small PBH fractions,

$$M_\bullet = M_\bullet^{(0)} + \delta M_\bullet, \qquad \delta M_\bullet = O(f_{\rm PBH}). \tag{12.3}$$

Consequently,

$$\mathcal{M}^{5/3} = (\mathcal{M}^{(0)})^{5/3}\left[1 + \frac{5}{3}\frac{\delta\mathcal{M}}{\mathcal{M}^{(0)}} + O(f_{\rm PBH}^2)\right]. \tag{12.4}$$

At the population level,

$$\frac{\delta\Omega_{\rm GW}}{\Omega_{\rm GW}^{(0)}} = \frac{5}{3}\left\langle\frac{\delta\mathcal{M}}{\mathcal{M}^{(0)}}\right\rangle + \frac{\delta R_{\rm tr}}{R_0} + O(f_{\rm PBH}^2), \tag{12.5}$$

where the precise interpretation of $\delta R_{\rm tr}/R_0$ depends on the adopted population measure.

13. Falsifiability and relation to previous approaches

The framework makes a population-level prediction: if PBH transport substantially modifies SMBH growth, it should generally modify the distribution of response-weighted GW sources. The monopole test constrains $\Omega_{\rm GW}(f)$, while the anisotropy test constrains $C_\ell(f)/C_0(f)$. A PBH parameter region that matches the spectrum but predicts excessive anisotropy can therefore be rejected.

The construction differs from an amplitude-only correction. A multiplicative change in $\Omega_{\rm GW}$ leaves normalized source weights unchanged, whereas PBH transport changes the mass and residence-time distribution entering $W_i(f)$. The joint statistic in Eq. (7.12) is intended to expose this distinction.

The approach also complements recent work on PBH contributions to the SGWB [10] and on SMBHB anisotropy [14]. The former emphasizes the spectral amplitude produced by PBH-assisted central growth, while the latter demonstrates that source discreteness and environmental evolution affect angular statistics. The present formulation connects the two through a common transport operator.

14. Limitations and reproducibility

The transport efficiency $\eta_{\rm df}$ is uncertain because PBH orbital distributions, halo density profiles, velocity distributions, and the Coulomb logarithm are not precisely known. The mapping

$$M_\bullet \longrightarrow (M_1, M_2) \tag{14.1}$$

also requires a pairing, merger-efficiency, and mass-ratio prescription.

Environmental residence times may be degenerate with the PBH effect because both mechanisms can change the spectral shape and angular source weights. Spatial anisotropy cannot be inferred from the one-point mass function alone; a realization of source positions is required.

The present paper does not claim a fit to PTA data. The equations and algorithm define a computational framework that can be coupled to a PTA likelihood in a subsequent analysis. Any observational inference should propagate uncertainty in halo histories, transport efficiency, merger prescriptions, environmental hardening, and source positions.

For reproducibility, a numerical study based on this manuscript should report: the cosmological parameters, halo-mass and redshift ranges, time and frequency grids, kernel parameters, transport efficiency prescription, merger prescription, environmental model, convergence tolerances, random-number seed, number of population realizations, and the values of N_t, N_s, and $\ell_{\max}$. These quantities determine the numerical error and the Monte Carlo sampling error separately.

15. Conclusions

We have reformulated PBH-assisted SMBH assembly as a causal transport problem with an explicit computational realization. The central response is represented by the Volterra operator $\mathcal{V}$, which maps the PBH transport source into the central black-hole growth history. Under a normalized nonnegative kernel, the operator is stable in the sup norm, while a composite trapezoidal discretization gives an explicit consistency estimate. A sequential predictor–corrector scheme provides a reproducible baseline solver.

The resulting population pipeline maps the evolved central mass into binary masses, chirp masses, residence times, source weights, the SGWB spectrum, angular multipoles, effective source number, and the joint statistic J_ℓ. Direct memory evaluation scales quadratically with the number of time nodes, whereas a positive finite exponential representation reduces the memory update to linear complexity in the number of time nodes for fixed kernel rank.

The astrophysical closures remain phenomenological and should be replaced by more detailed population prescriptions when data are analyzed. The mathematical and computational contribution of the present work is the causal operator formulation, its stability properties, the discretization and error controls, and the modular source-to-observable algorithm. The no-PBH limit and limiting transport regimes provide internal validation tests.

The framework therefore supplies a concrete route for testing whether a PBH-induced modification of SMBH assembly can simultaneously alter the SGWB spectrum and its angular anisotropy. Such a joint test is more informative than an amplitude-only comparison because the same evolved source population controls both observables.

Acknowledgement

The author thanks the gravitational-wave and cosmology communities for publicly available theoretical and observational results that motivate this work. The author also acknowledges that the manuscript was prepared with AI-assisted language and formatting support, used under author supervision for clarity and readability; all scientific content, calculations, references, and final editorial decisions remain the responsibility of the author.

References

[1] Agazie, G., et al. (NANOGrav Collaboration) (2023). The NANOGrav 15-year data set: Evidence for a gravitational-wave background. *Astrophysical Journal Letters*, 951, L8. https://doi.org/10.3847/2041-8213/acdac6

[2] Antoniadis, J., et al. (2023). The second data release from the European Pulsar Timing Array: III. Search for gravitational wave signals. *Astronomy & Astrophysics*, 678, A50. https://doi.org/10.1051/0004-6361/202346844

[3] Begelman, M. C., Blandford, R. D., & Rees, M. J. (1980). Massive black hole binaries in active galactic nuclei. *Nature*, 287, 307–309. https://doi.org/10.1038/287307a0

[4] Carr, B. J., & Hawking, S. W. (1974). Black holes in the early Universe. *Monthly Notices of the Royal Astronomical Society*, 168, 399–415. https://doi.org/10.1093/mnras/168.2.399

[5] Chandrasekhar, S. (1943). Dynamical friction. I. General considerations. *Astrophysical Journal*, 97, 255–262. https://doi.org/10.1086/144517

[6] Chapline, G. F. (1975). Cosmological effects of primordial black holes. *Nature*, 253, 251–252. https://doi.org/10.1038/253251a0

[7] Hawking, S. (1971). Gravitationally collapsed objects of very low mass. *Monthly Notices of the Royal Astronomical Society*, 152, 75–78. https://doi.org/10.1093/mnras/152.1.75

[8] Hellings, R. W., & Downs, G. S. (1983). Upper limits on the isotropic gravitational radiation background from pulsar timing analysis. *Astrophysical Journal Letters*, 265, L39–L42. https://doi.org/10.1086/183954

[9] Lacey, C., & Cole, S. (1993). Merger rates in hierarchical models of galaxy formation. *Monthly Notices of the Royal Astronomical Society*, 262, 627–649. https://doi.org/10.1093/mnras/262.3.627

[10] Martín-González, D. (2026). Primordial black hole contribution to the stochastic background of gravitational waves. *Astronomy & Astrophysics*, 713, A19. https://doi.org/10.1051/0004-6361/202660487

[11] Oyefusi, A. S., Odetunde, O. S., Onitilo, S. A., & Adepoju, J. T. (2026). Operator theoretic analysis of coupled decomposition methods. *Annals of Mathematics and Computer Science*, 36. https://doi.org/10.56947/amcs.v36.926

[12] Padhy, B., Mahapatra, P. S., & Samantara, T. (2026). Adaptive hybrid B-spline PINN for fractional equations. *Annals of Mathematics and Computer Science*, 35. https://doi.org/10.56947/amcs.v35.864

[13] Peters, P. C. (1964). Gravitational radiation and the motion of two point masses. *Physical Review*, 136, B1224–B1232. https://doi.org/10.1103/PhysRev.136.B1224

[14] Raidal, J., Urrutia, J., Vaskonen, V., & Veermäe, H. (2026). Statistics of supermassive black hole gravitational wave background anisotropy. *Astronomy & Astrophysics*, 706, A159. https://doi.org/10.1051/0004-6361/202453516

[15] Reardon, D. J., et al. (2023). Search for an isotropic gravitational-wave background with the Parkes Pulsar Timing Array. *Astrophysical Journal Letters*, 951, L6. https://doi.org/10.3847/2041-8213/acdd02

[16] Shirole, Y., & Jodand, S. M. (2026). New approach for analysis of solution of certain fractional sum-difference equations. *Annals of Mathematics and Computer Science*, 35. https://doi.org/10.56947/amcs.v35.837

[17] Xu, H., et al. (CPTA Collaboration) (2023). Searching for the nano-Hertz stochastic gravitational-wave background with the Chinese Pulsar Timing Array. *Research in Astronomy and Astrophysics*, 23, 075024. https://doi.org/10.1088/1674-4527/acdfa5

[1] Department of Mathematics, Manipur International University, Ghari, Imphal 795140, India.

Email address: bhaktarajthiyam3076@gmail.com